Thin-Walled Structures 86 (2015) 83–93

Contents lists available at ScienceDirect

Thin-Walled Structures

journal homepage: www.elsevier.com/locate/tws

Crushing and energy absorption characteristics of combined geometry shells at quasi-static and dynamic strain rates: Experimental and numerical study

Alper Tasdemirci *, Selim Sahin, Ali Kara, Kivanc Turan

Dynamic Testing and Modeling Laboratory and Department of Mechanical Engineering, Izmir Institute of Technology, Gulbahce, Urla, Izmir, Turkey

ARTICLE INFO

Article history:
Received 11 August 2014
Received in revised form
12 September 2014
Accepted 15 September 2014
Available online 31 October 2014

Keywords:
Combined geometry shells
Crushing behavior
Energy absorption
Micro inertia
Finite element method

ABSTRACT

The quasi-static and dynamic crushing response and the energy absorption characteristics of combined geometry shells composed of a hemispherical cap and a cylindrical segment were investigated both experimentally and numerically. The inelastic deformation of the shells initiated with the inversion of the hemisphere cap and followed by the axisymmetric or diamond folding of the cylindrical segment depending on the loading rate and dimensions. The fracture of the thinner specimens in dynamic tests was ascribed to the rise of the flow stress to the fracture stress with increasing strain rate. The hemisphere cap absorbed more energy at dynamic rates than at quasi-static rates, while it exhibited lower strain rate and inertia sensitivities than the cylinder segment. For both the hemisphere cap and the cylinder segment, the inertial effect was shown to be more pronounced than strain rate effect at increasing impact velocities.

1. Introduction

The combined geometry shells with the combinations of such as cylindrical, spherical and conical shapes are widely employed in engineered structures, the examples of which may include the nose-cone of aircrafts and projectiles and the shape of fuel and gas tanks and pressure hulls. The superior energy absorption characteristics of combined geometry shells lie in the crushing behavior of their constituents. These structures crush progressively, mostly in planar form, under static and dynamic compressive loads, leading to relatively high efficiency of the conversion of kinetic energy into irreversible plastic deformation energy. Determination of the crushing mechanisms and energy absorption characteristics of these structures under various loading conditions and deformation rates are important to assure the required protection level by energy absorption without any damage on the protected structures.

One of the earliest studies on the thin-walled cylindrical tubes was performed by Alexander [1]. Alexander proposed an analytical model for predicting the average axisymmetric crushing loads of thin-walled tubes. The tubes with low D/t ratios (diameter/wall-thickness) and rigidly perfectly plastic materials tend to exhibit axisymmetric mode (concertina) of deformation [2], while the tubes with high D/t ratios and strain hardening materials exhibit asymmetric mode (diamond) of deformation [3]. The effect of foam-filling and end-constraining on the crushing behavior of thin-walled tubes has been investigated widely, the examples of which include Santosa et al. [4], Güden and Kavi [5] and Singace and El-Sobky [3]. A coupled experimental and numerical study on the quasi-static crushing of tubes was performed by Taşdemirci [6]. The crush behavior of segmented thin-walled tubes was investigated in a recent study by Shahi and Marzbanrad [7]. Updike [8] investigated large compression deformation of a rigid-plastic spherical shell and proposed an analytical model relating the crushing force to the deformation. De Oliveira and Wierzbicki [9] derived closed form solutions for conical and spherical shells subjected to point and boss loading. The solutions were reported valid until the crush distance reached the spherical shell radius. Gupta et al. [10] investigated the buckling of thin spherical shells under axial loads. The deformation history of thin spherical shells was divided into three modes distinguished in the load-deformation history as the decreasing slopes; local flattening, axisymmetric inward dimpling, and asymmetric lobe formation. Quasi-static and dynamic crushing and deformation behavior of metallic spherical shells were investigated by Gupta and Venkatesh [11], Gupta and Gupta [12] and Gupta et al. [13] for different loading rates. The collapse behavior of the arrays of ping-pong balls were investigated both experimentally and numerically by Ruan et al. [14], Dong et al. [15], and Bao and Yu [16].

Although, there have been quite many studies on the static and dynamic crushing behavior of tubes, spheres, hemispheres, and cones, few examples of which are broadly outlined above; there have been few experimental and numerical studies in the

* Corresponding author. Tel.: +90 232 7506780; fax: +90 232 7506701.
E-mail address: alpertasdemirci@iyte.edu.tr (A. Tasdemirci).

http://dx.doi.org/10.1016/j.tws.2014.09.020
0263-8231/

literature on the static and dynamic crushing of the combinations of these geometries. Ghamarian and Abadi [17], Ghamarian et al. [18] and Ghamarian and Zarei [19] investigated the energy absorption characteristics of empty and foam-filled circular and conical end-capped tubes and showed that the absorbed energy increased with increasing impact velocity. Gupta [20] investigated the static deformation behavior of tube-frusta combined geometry experimentally and numerically. The mode of collapse was observed by a development of one concertina fold and followed by a plastic zone. Ghamarian et al. [21] used shallow spheres as end-cap in conical tubes. The crush force efficiency and absorbed energy was reported to increase with increasing shallow spherical cap radius. Shojaeefard et al. [22] studied the quasi-static crushing behavior of combined cylindrical and square section tubes and showed that the absorbed energy of the combined tubes was slightly higher than both square and circular tubes of the same length.

The aim of the current study is to determine both experimentally and numerically the energy absorption characteristics and crushing behavior of the combined geometry shells (hemispherical cap and cylindrical segment) at quasi-static and high strain rates. This study is a part of an experimental and numerical work on the investigation of the use of combined geometry shells in the structures designed specially against blast and impact loading. The consistency between the experimental and numerical results showed that the numerical methodology followed in this study can further be used to predict the deformation modes and energy absorption behavior of sandwich structures.

2. Experiments and modeling

2.1. Materials and testing

The investigated non-standard size combined geometry shells were prepared by deep-drawing 0.5 and 1 mm thick AISI 304L stainless steel sheet blanks between punch and die. The tooling for the deep-drawing process was machined locally for the present study. The edge of the deep drawn cylindrical segment on the bottom side formed during the forming process was trimmed by a cutting tool on a CNC lathe. The prepared specimens of various configurations commonly consisted of a hemispherical cap and a cylindrical segment. Four different combined geometry shell configurations were tested and modeled. The coding of the configurations is as follows: S1X, S2X, B1X and B2X. The first letters, S and B, refer to the sample's radius. The samples 15 mm in diameter are coded as S (small) and the samples in 25 mm diameter as B (big). The pictures of prepared small and big radius combined shells are shown in Fig. 1. The numbers after the first letters, 1 and 2, refer to the sample thickness of 0.5 and 1 mm, respectively. The last number in the coding, X, represents the type of the test applied. The quasi-static test is coded as 1 and drop-weight test as 2. The code of B12, for example, refers to a sample with 12.5 mm diameter and 0.5 mm thickness, tested in drop-weight.

The tested drawn combined geometry shells are noted to show variations in wall thickness due to the nature of applied deep drawing process, which stretches the blanks over the die surface at the edges inhomogeneously. To assess the wall thickness variations in the section walls, the applied deep drawing process was simulated in LS-DYNA 971 and the resultant thickness variations were assessed numerically. The numerically determined thicknesses were then compared with the experimentally measured thicknesses on the shell wall segments.

For the numerical model of the applied deep-drawing process, the elastic and plastic deformation behaviors of as-received AISI 304L stainless steel sheets were determined at quasi-static and high strain rates. The quasi-static tension tests were performed in accord with ASTM E8M-04 standard at the strain rates of 10^{-3}, 10^{-2} and $10^{-1}\,s^{-1}$ using a Shimadzu universal test machine and high strain rate tension tests were conducted in a tensile Split Hopkinson Pressure Bar (SHPB) at the average strain rates of 1100 and $1400\,s^{-1}$. The details of the used 316L stainless steel bar tensile SHPB and the methodology of extracting material constitutive equation are given elsewhere [23]. The axial displacements of quasi-static test specimens were recorded using a video extensometer, while a high speed camera was used to monitor the deformation during the SHPB tension tests. Typical quasi-static and high strain rate true stress-true plastic strain curves of AISI 304L stainless steel are shown in Fig. 2. The tested stainless steel shows a strong strain rate dependent flow stress as seen in Fig. 2. The yield stress increases from about 230 MPa at quasi-static strain rate to about 475 MPa at high strain rate. The fracture strain is also found strain rate dependent; the fracture strain decreases from about 0.6 at quasi-static strain rate to about 0.3 at high strain rate. As elaborated in detail in the modeling section, a constitutive model incorporating the effect of strain rate on both strength and failure strain was used in the simulations.

In the quasi-static compression testing ($1 \times 10^{-3}\,s^{-1}$) of the combined geometry shells two different cross-head speeds were implemented: 13 mm-high combined geometry shell specimens were compressed at a cross-head speed of 0.78 mm min^{-1}, while 23 mm-high specimens were compressed at a cross-head speed of 1.38 mm min^{-1}. Low velocity impact tests were conducted in a Fractovis drop-weight tower (Fig. 3). The main constituents of the drop-weight tester include striker holder, striker weights and striker tip. The striker was attached to a 90 kN strain-gaged sensor. The tests were conducted using a flat end striker tip and the striker velocity

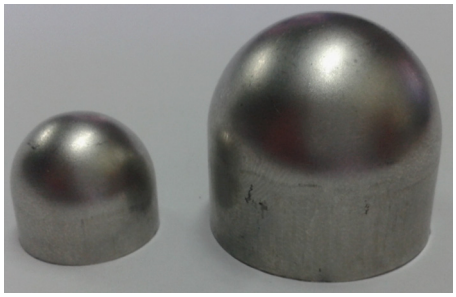

Fig. 1. Small and big radius combined geometry shells.

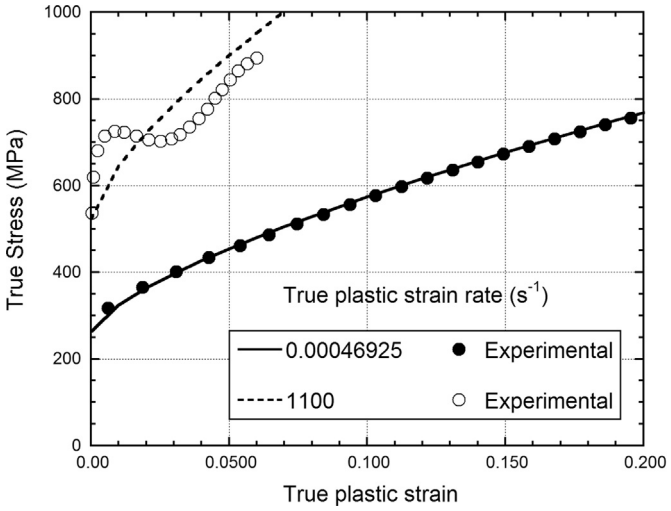

Fig. 2. Experimental tensile stress–strain curves of AISI 304L steel at quasi-static and high strain rates and corresponding Johnson–Cook model fits.

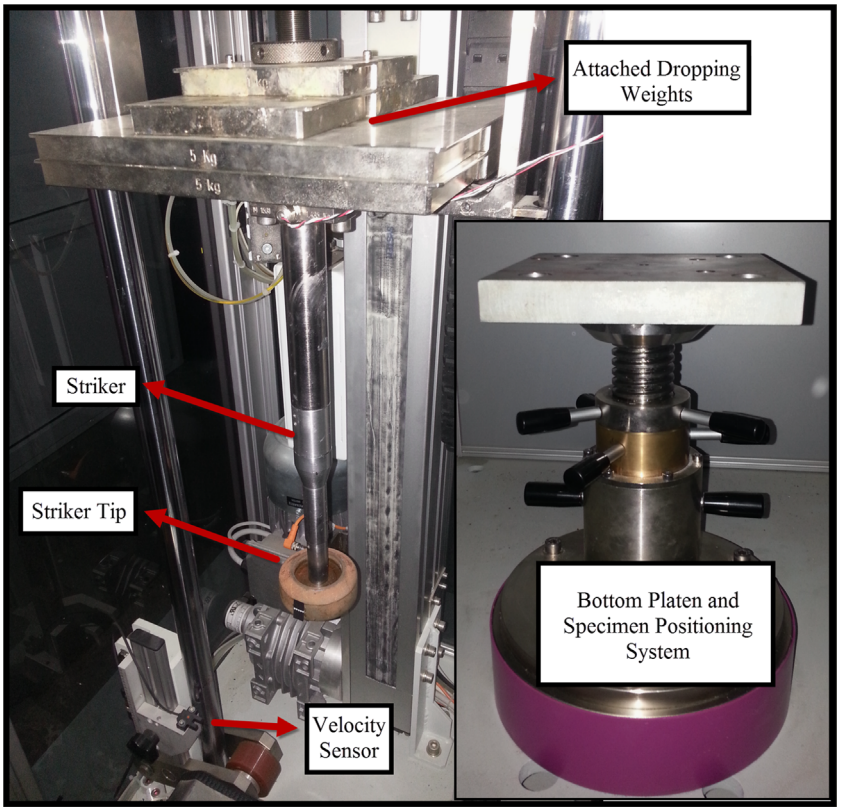

Fig. 3. Drop-weight test apparatus.

Table 1
Experimental and numerical results.

Specimen	Dimensions			Drop mass (kg)	Result	P_i (kN)	P_{max} (kN)	P_m (kN)	Energy (J)	*SAE* (kJ/kg)	Compression (mm)
	R (mm)	t (mm)	L (mm)								
S11	7.5	0.5	13.01	–	Experimental	14.8	14.8	7.9	79.3	39.6	10.0
					Numerical	14.3	14.3	8.1	90.0	45.0	11.1
S12	7.5	0.5	13.05	10.4	Experimental	14.9	16.2	8.5	96.5	48.2	11.3
					Numerical	16.5	19.9	10.9	124.3	62.2	11.4
S21	7.5	1.0	13.06	–	Experimental	62.7	62.7	33.3	323.6	107.9	9.7
					Numerical	52.7	60.1	32.9	348.1	116.0	10.6
S22	7.5	1.0	13.02	23.4	Experimental	34.8	48.8	27.1	289.3	96.4	10.7
					Numerical	51.1	63.3	27.2	272.5	90.8	10.0
B11	12.5	0.5	23.06	–	Experimental	15.5	19.6	10.7	203.8	34.0	19.0
					Numerical	17.0	19.8	11.5	220.2	36.7	19.1
B12	12.5	0.5	22.8	7.4	Experimental	15.4	23.0	9.3	189.7	31.6	20.5
					Numerical	19.6	26.1	13.9	282.2	47.0	20.4
B21	12.5	1.0	22.62	–	Experimental	59.8	64.0	33.9	600.0	50.0	17.7
					Numerical	59.7	64.2	35.0	666.3	55.5	19.0
B22	12.5	1.0	22.95	14.4	Experimental	56.1	77.1	33.5	525.1	43.8	15.7
					Numerical	60.1	73.0	35.6	563.5	47.0	15.8

was measured by the photocells. The absorbed energy was internally calculated by integrating the force–displacement curves. The dimensions and results of quasi-static and drop-weight tests of the tested shell specimens are tabulated in Table 1. In this table, P_i is the initial peak load (for hemispherical cap), P_{max} is the maximum load, P_m is the mean load and *SAE* is the specific absorbed energy.

2.2. Modeling

The deep drawing of AISI 304L stainless steel and the quasi-static/dynamic compression of the combined geometry shells was modeled in LS-DYNA 971. As the crushing modes of the tested combined geometry shells were not axisymmetric, the shells were modeled in full geometry. The finite element model of the deep-drawing of steel blank is shown in Fig. 4(a). The model consisted of punch, blank holder, forming die and blank. The blank was modeled using Belytschko–Tsay shell element with seven integration points through the thickness. The optimum number of elements was determined by conducting a mesh sensitivity analysis. The analysis showed that an element size of 0.5 mm converged to the solutions within a reasonable time. In the simulations, the displacement control curve with a trapezoidal velocity profile was used as input. Since, the displacement rates were relatively low for an explicit solver, the mass-scaling [4] was applied in order to obtain reasonably small time steps and speed up the solution. The density of blank material was scaled down by

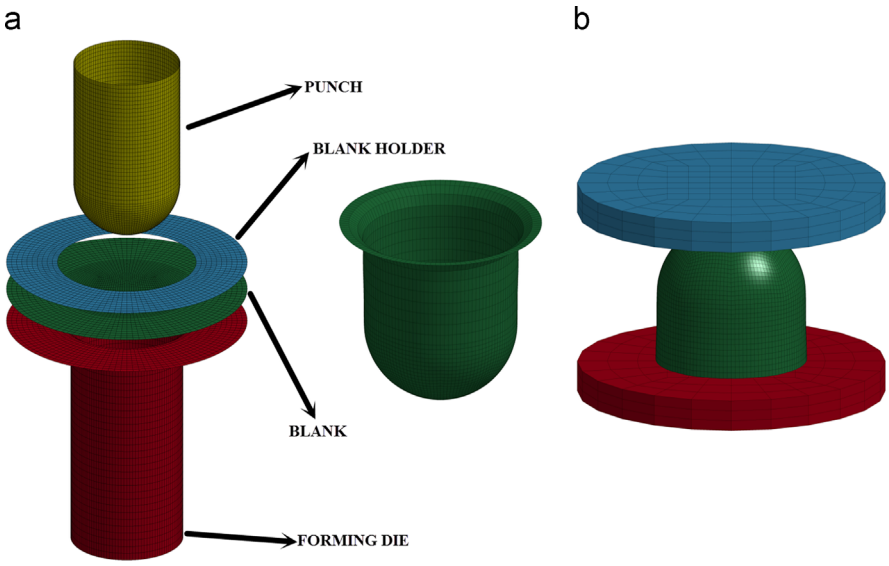

Fig. 4. Model of (a) deep drawing process and (b) the quasi-static and dynamic compression of the combined shell.

Table 2
Johnson–Cook model properties of AISI 304L stainless steel used in numerical models.

ρ (kg/m^3)	G (GPa)	E (GPa)	υ	A (MPa)	B (MPa)	n	C	$D1$	$D4$
7830	80	193	0.305	264	1567.33	0.703	0.067	0.53467	−0.01913

a factor of 1000 and the tool (punch) velocity was set at 10 m s^{-1}. With the mass-scaling, the ratio of kinetic energy to total internal energy was less than 4% over the period of deep drawing process, ensuring quasi-static strain rates. Contact one way forming surface to surface definition was used to account for the contact between the tooling and blank material. A static friction coefficient of 0.15 and a dynamic friction coefficient of 0.1 between all surfaces in-contact were assumed in the numerical model. The combined geometry shells may retain significant amount of residual strain and stress following the deep-drawing process. LS-DYNA 971 allows users to perform follow-on simulations such as trimming and additional forming. For this purpose, the "dynain" file generation methodology ([24, 25]) was followed. This dynain file was included into a new LS-DYNA 971 input deck for quasi-static and dynamic crushing simulations. In the simulations, die, punch and blank holder were modeled rigid and the blank deformation was modeled using the Johnson–Cook (J–C) material model. In this material model, the equivalent stress (σ_{eq}) is expressed as

$$\sigma_{eq} = (A + B\varepsilon_{eq}{}^{n})\left(1 + C\ln\left(\dot{\varepsilon}^{*}_{eq}\right)\right)(1 - T^{*m}) \tag{1}$$

where, ε_{eq} is the equivalent plastic strain and A, B, n, C and m are the material constants. The dimensionless plastic strain rate ($\dot{\varepsilon}^{*}_{eq}$) is given by $\dot{\varepsilon}^{*}_{eq} = (\dot{\varepsilon}_{eq}/\dot{\varepsilon}_0)$, where $\dot{\varepsilon}_0$ is a user defined reference strain rate, and ($\dot{\varepsilon}_{eq}$) is the equivalent plastic strain. The homologous temperature (T^*) is defined as $T^* = (T - T_r)/(T_m - T_r)$, where T is the absolute temperature, T_r is the room temperature and T_m is the melting temperature.

The failure model considered in this study is based on Johnson–Cook damage model. According to Johnson–Cook damage model, strain at fracture can be written as follows:

$$\varepsilon_f = \left[D_1 + D_2 e^{D_3\sigma^*}\right]\left[1 + D_4 \ln\left(\frac{\dot{\varepsilon}}{\dot{\varepsilon}_0}\right)\right][1 + D_5 T^*] \tag{2}$$

where D_1, D_2, D_3, D_4 and D_5 are damage parameters, $\sigma^* = \sigma_m/\sigma_e$ is stress triaxiality ratio. In the current study, the stress state does not vary significantly during compression. Thus, the following simplified form concentrating only on the strain rate dependency was considered.

$$\varepsilon_f = D_1\left[1 + D_4 \ln\left(\frac{\dot{\varepsilon}}{\dot{\varepsilon}_0}\right)\right] \tag{3}$$

Note also that, thermal effects on both material and damage models were neglected. The determined J–C material and damage model constants of AISI 304L stainless steel are tabulated in Table 2.

The finite element model of the quasi-static and dynamic compressions of the combined geometry shell is shown in Fig. 4(b) and consists of a moving rigid upper plate, specimen and stationary rigid lower plate. In the quasi-static simulations, the upper plate moved with the cross-head velocity only along the loading direction while the lower plate was fully constrained in all directions. In the drop-weight simulations, the top rigid plate moved on its axis with a downward velocity by the fall of dropping weight and node based mass lumping methodology was followed in order to match the total weight of the drop-weight tester cross-head. Two different types of contacts were used in the numerical model. For the combined geometry shell itself, an eroding single surface contact was used to account for the contact between folds during the deformation and new contact interface was created due to the erosion, if there was any. While an eroding surface to surface contact was applied between the combined geometry and rigid top/bottom plates. A static friction coefficient of 0.3 and a dynamic friction coefficient of 0.2 between the contact surfaces were assumed in the numerical study. Once the numerical model was verified then the numerical study was extended in order to reveal the effects of inertia and base material's strain rate sensitivity on the deformation behavior of combined geometry shells. In order to distinguish the discrete effect of these factors, the numerical models were rerun for the strain rate insensitive base material. The results of the strain rate-sensitive and insensitive base material models were then compared for quasi-static and dynamic crushing.

3. Results and discussion

3.1. Experimental and numerical

The measured and numerical thickness variations of the shells as function of the distance from apex are shown in Fig. 5a and b for S2X and B2X combined geometry shells, respectively. Close agreements between the measured and numerical thicknesses are seen for both combined geometry shells, except the sections between hemisphere cap and cylindrical segment. At these locations the measured thickness values are greater than the numerically determined thicknesses, while the difference between them is also more marked for B2X samples. Also, the combined shell geometry is relatively thinner in the hemisphere cap compared to cylindrical segment (Fig. 5a and b). The difference between the measured and numerical thickness values may arise from the use of a constant friction coefficient in the simulations, while in the actual deep-drawing process the friction coefficient may change locally with the deformation, particularly at the locations of curved or stepped sections. The increased friction coefficient particularly between hemisphere and cylindrical segment during the course of deep-drawing process may induce relatively non-uniform deformation leading to deviations between the measured and numerically determined thicknesses. Nevertheless, the numerical results clearly indicate the general trends of thickness variations of the shells and the largest variations in the measured thicknesses are seen in the hemisphere cap.

Fig. 6a and b shows sequentially typical quasi-static and drop-weight load–displacement curves of B1 specimen. In the inset of the same figure, the sequences of the deformation of the sample corresponding to the displacements marked with the dots are also shown. The inelastic deformation in quasi-static test starts following the elastic deformation of the shell. Initially, the hemi-spherical cap is flattened until about the first peak force (10 mm) as seen in Fig. 6a.

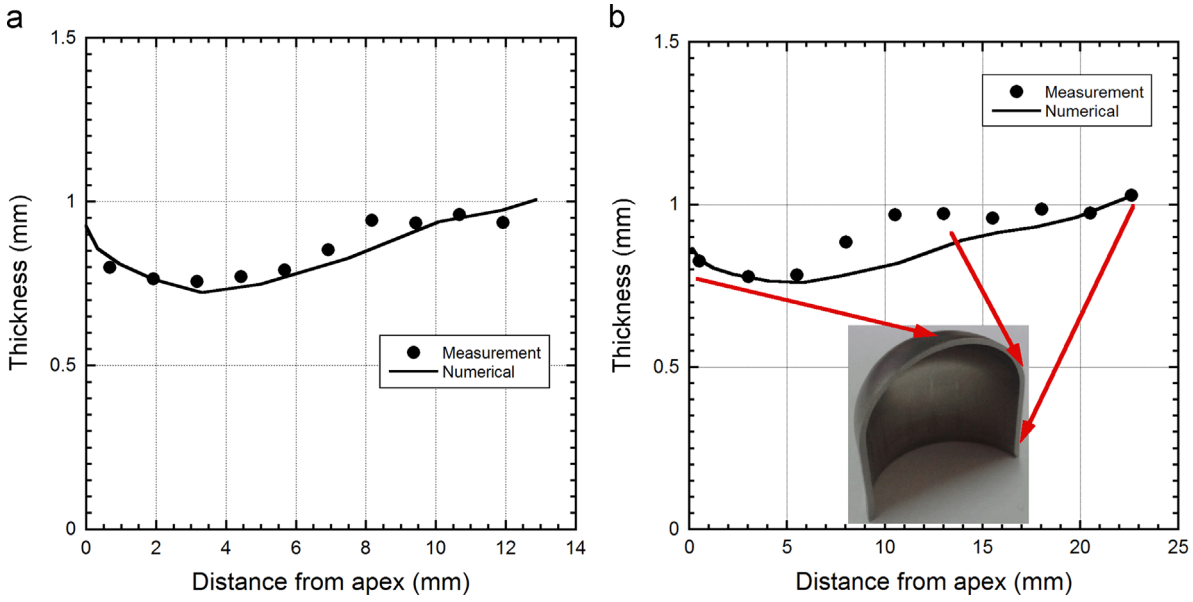

Fig. 5. Measured and experimental thickness vs. distance from apex graphs for deep drawing of (a) S2X and (b) B2X combined geometry shell.

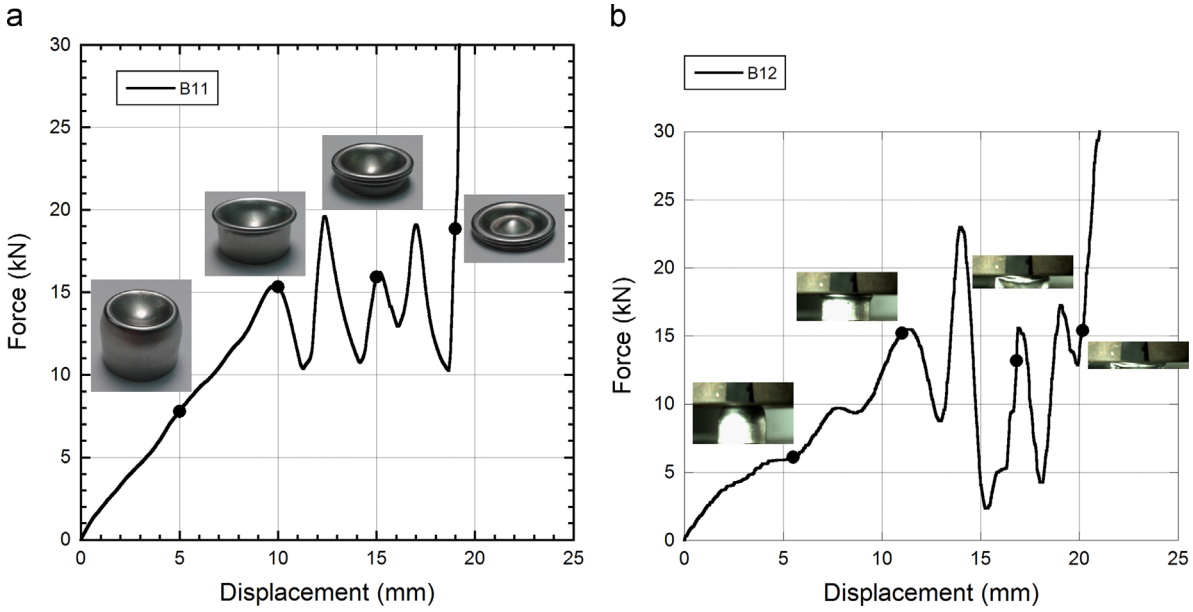

Fig. 6. Force–displacement curves of (a) B11 and (b) B12 combined geometry shell samples.

This results in an almost linear force–displacement behavior. Following the initial peak load, that shows the flattening of the hemi-spherical cap, the deformation proceeds with the axisymmetric folding of the cylindrical segment. The following peak loads corresponds to the initiation and completion of the sequential folding. Both experimentally and numerically two folds are formed in the cylindrical segment. The first fold is completed at 12.5 mm and the second fold at 17.5 mm displacement. At the later stages of the deformation, just before the completion of the second fold, the inversion of the hemisphere cap occurs (15 mm). This is reflected as the peak force occurrence between the completion of first and second axisymmetric folds. Following the completion of the second fold after 18.5 mm displacement, the crushed section is compressed altogether, leading to sharp increase in the force values. The plastic deformation under dynamic loading also starts with the flattening of the hemi-spherical cap and following axisymmetric folding (Fig. 6b). Although the first fold formation is axisymmetric in these tests, the following second folding is reverted to the diamond mode. The deformation mode change is also reflected in the force–displacement curve of dynamically tested shell shown in Fig. 6b. The initial and the following peak forces of dynamically tested specimen are greater than that of quasi-statically tested specimen, the later peaks are reduced to that of quasi-statically tested specimen. The decline in the force values is due to subsequent generation of the diamond mode of deformation. The dynamically tested specimens, as with quasi-statically tested specimens, deform in the cylindrical segment by forming two folds; one axisymmetric and one diamond. The diamond mode of deformation is a lower mode and leads to reduced average crushing forces [26]. It is known that the axisymmetric fold formation is an upper mode deformation of diamond mode and occurs predominantly at high strain rates [26], while an opposite result is observed in the present study. Noting also that the control of the specimen alignment in quasi-static tests is easier than dynamic drop-weight testing, the change of deformation mode of tested shells

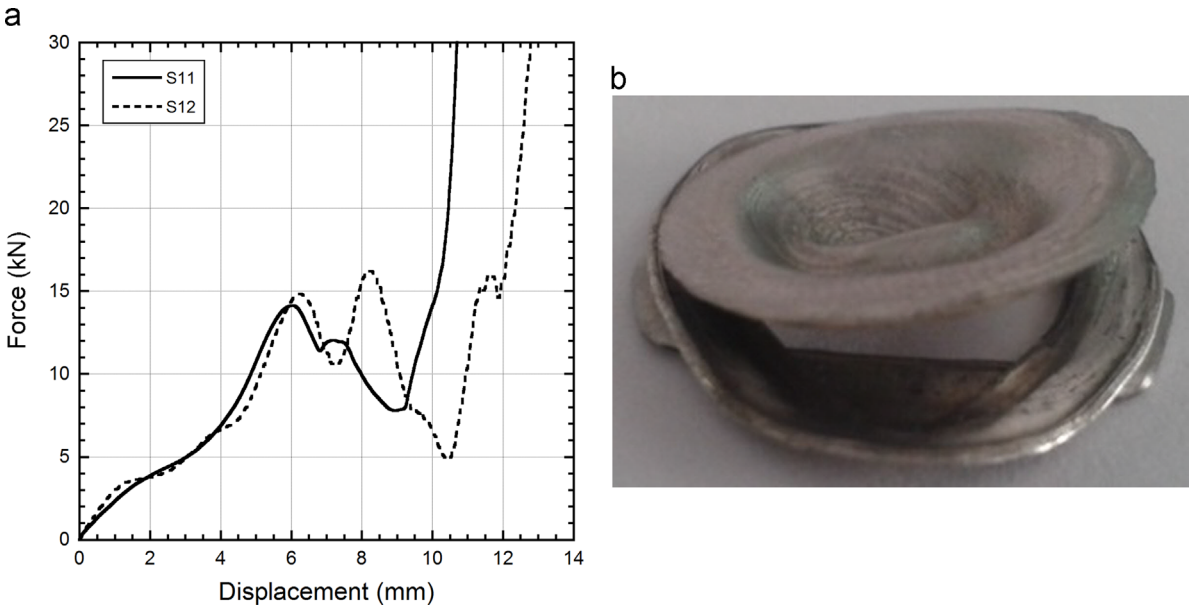

Fig. 7. Force–displacement curves of (a) S11 and S12 samples and (b) the picture of the deformed S12 sample.

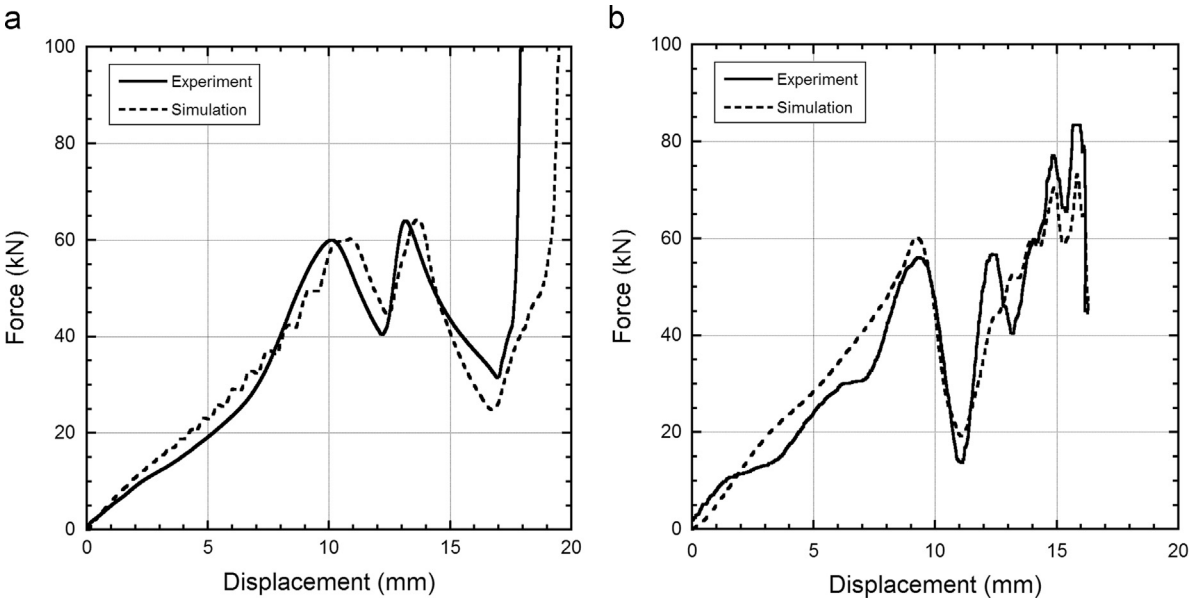

Fig. 8. Experimental and numerical force–displacement curves of (a) B21 and (b) B22 combined geometry shell samples.

at high strain rates is ascribed to the experimental artifacts of drop-weight testing such as misalignment of the specimen during the test.

As tabulated in Table 1, the maximum load value in drop weight test (23 kN) is 18% greater than that of quasi-static test (19.6 kN). This maximum load occurs at the completion of the first axisymmetric mode (Fig. 6b), while with the start of the initiation of the following diamond mode, a large drop in load values are seen in Fig. 6b. The average force value at quasi-static test is higher than that of drop weight test, leading to higher SAE value in quasi-static test. Similar experimental load–deformation graphs are also observed for S1specimen for quasi-static and drop weight tests as shown in Fig. 7a. The deformation mode is however diamond fold formation at both quasi-statically and dynamically tested specimens, while dynamically tested specimen fractures at around 6 mm displacement. The relatively thinner section wall thickness of S1X samples as compared with B1X sample induced diamond mode of deformation. Similar section wall effects were also found in the axial crushing of metal tubes [26]. The fracture of the dynamically deformed sample is due to the increase of the flow stress of AISI 304L steel with increasing strain rate to the point of the fracture stress. The fracture starts right before the first fold initiation at the cylindrical segment of the combined geometry and two separate portions are created accordingly, a flattened and inward fold hemi-spherical cap and cylindrical segment, see Fig. 7b. As seen also in Fig. 7a, only one fold is formed in S1 samples.

The experimental and numerical load–deformation curves of B2 specimens at quasi-static and dynamic strain rates are shown in Fig. 8a and b, respectively. The static and dynamic numerical load–deformation curves show close agreements with the experimental curves. The numerical static and dynamic average crushing loads are sequentially 35 kN and 35.6 kN, which are comparable

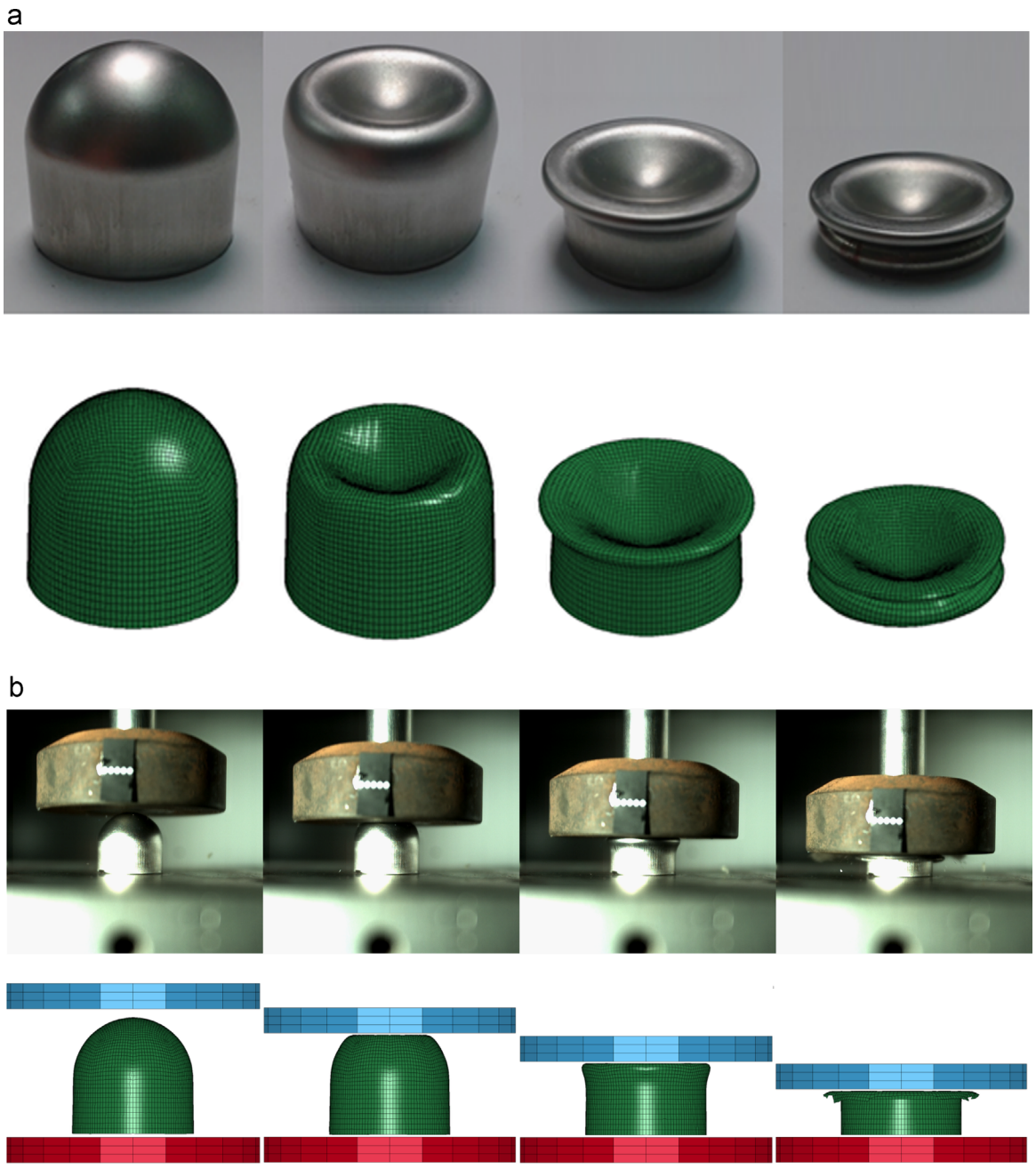

Fig. 9. Experimentally and numerically deformed pictures of (a) B21 and (b) B22 specimens.

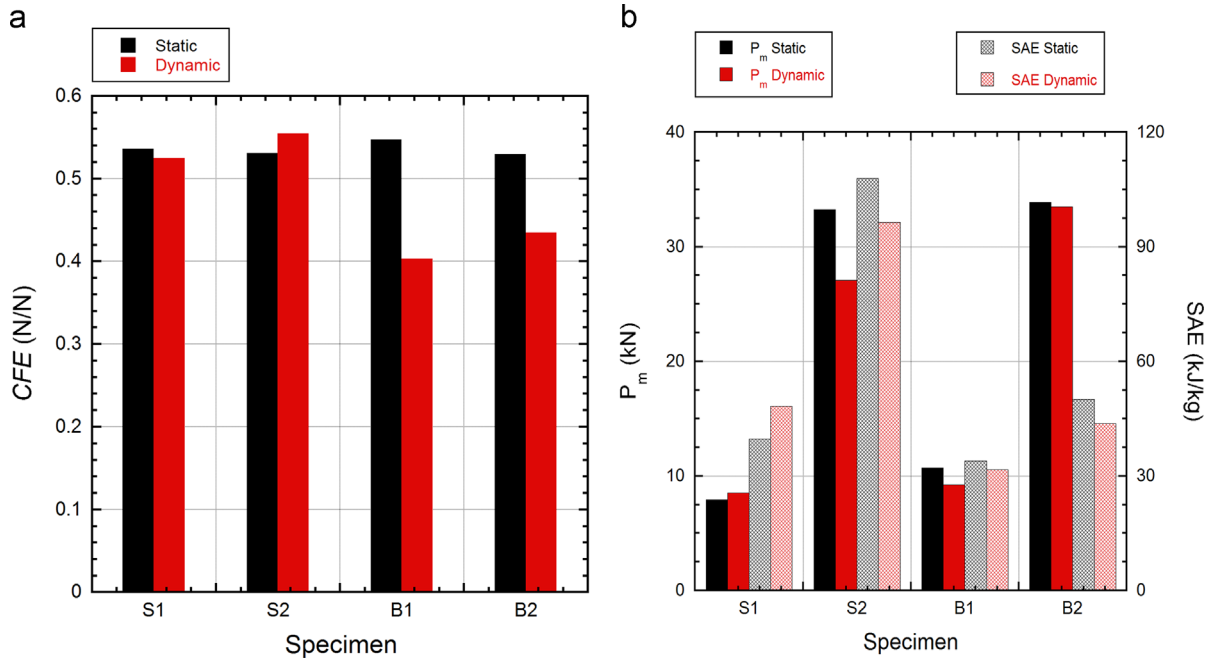

Fig. 10. (a) Static and dynamic CFE and (b) mean force and SAE.

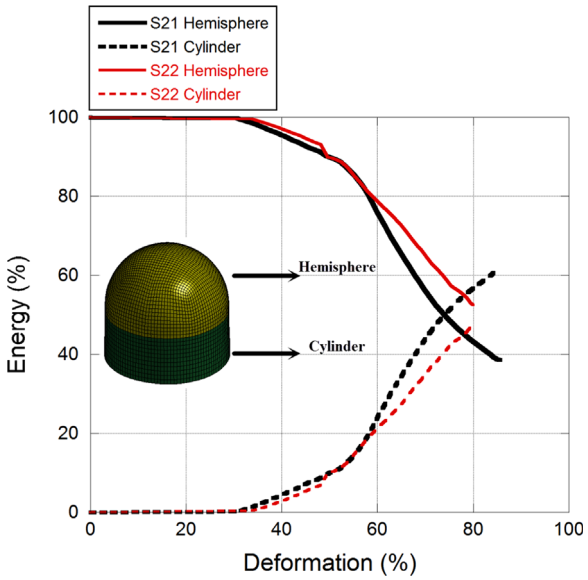

Fig. 11. Energy partitions between the hemisphere and cylinder segments of S2 specimen at quasi-static and dynamic strain rates.

with the experimental values, 33.9 kN and 33.5 kN, respectively. Experimentally and numerically deformed pictures of B2 specimens at static and dynamic strain rates are sequentially shown in Fig. 9a and b. As with load–displacement curves, the simulated deformation patterns of B2 samples show very close resemblances with experiments at quasi-static and dynamic strain rates. Both, experimentally and numerically deformed dynamic specimens fracture after the hemi-spherical segment is flattened and folded inwardly (Fig. 9b). After that, the sample breaks in two pieces; top flattened hemi-spherical cap and cylindrical segment. At the later stages of the deformation, cylindrical bottom segment buckles and folds. The fracture is reflected as the sudden load drop after the initial peak load (~9 mm displacement) in the load–displacement curve shown in Fig. 8b.

Among all the specimens tested in the current study, the highest P_i value is found in S21, whereas the lowest P_i value in S11 specimen. The highest P_{max} value is attained in B22, whereas the lowest P_{max} value in S11 specimen. In order for the higher energy absorption and protection efficiency, maximum load transmitted to the structure (P_{max}) should be minimized and to increase energy absorption capacity, the mean load value should be maximized. For this purpose, crushing force efficiency (*CFE*) parameter is calculated using the following relation:

$$CFE = \frac{P_m}{P_{max}} \tag{4}$$

The calculated *CFE* values of the quasi-statically and dynamically tested shells are summarized in Fig. 10a. As shown in Fig. 10a, *CFE* values vary between 0.4 and 0.55; S22 specimen shows the maximum, while B12 specimen shows the minimum *CFE* values. It is also noted that the *CFE* values at the quasi-static strain rates almost remain constant, while it increases at dynamic strain rates as the thickness of the shell increases. For the specimens of the same thickness, *CFE* values increase with increasing radius at quasi static strain rates. On the other hand *CFE* values decrease with increasing radius in dynamic loading. By investigating P_i, P_m and P_{max} values, the segment in which maximum load is observed can be detected. This information can be useful for optimization studies such as where buckling initiators can be placed etc. Fig. 10b summarizes mean load and *SAE* values of tested combined shell specimens. The highest *SAE* value is found in the quasi-statically tested S2 specimen and the lowest *SAE* value in dynamically tested B1 specimen. As the thickness of the specimen increases *SAE* values increase for all of the specimens. For the specimens having the same radius, as thickness increases, and P_m and *SAE* values increase. On the other hand, for the specimens of same thickness, as radius increases *SAE* values decrease and P_m values increase.

Fig. 11 shows the energy partitions between the hemisphere and cylinder segments of S2 specimen through the course of quasi-static and dynamic deformation. At both strain rates, almost all of the energy is absorbed by the hemispherical segment until about 35% deformation. After that, the cylindrical segment starts to deform and energy is equally shared by the hemisphere and cylinder segments at around 75% deformation. At the final stages

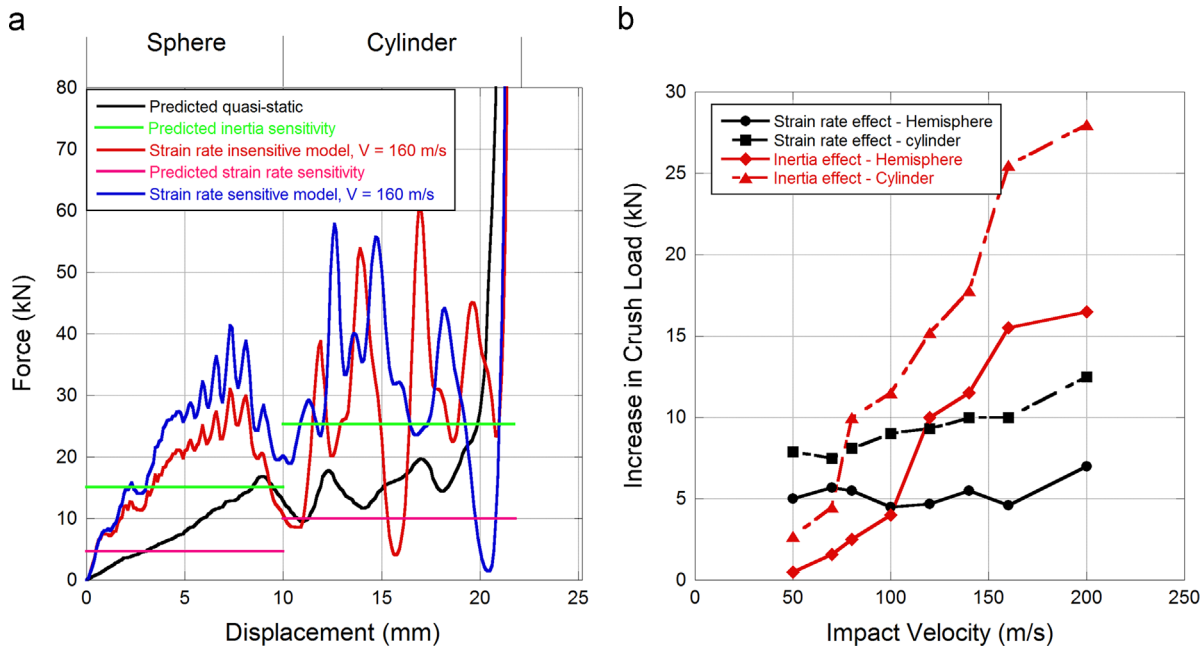

Fig. 12. (a) Strain rate and inertia effects for 160 m/s velocity and (b) increase in crush load vs. impact velocity.

of the deformation, energy sharing increases in the favor of cylindrical segment as the fold formation in the cylindrical segment occurs. It is also noted that the energy absorption by the hemispherical segment at high strain rate is greater than quasi-static strain rate. This is partly attributed to the inertial effects and partly to the strain rate sensitivity of AISI 304L steel.

3.2. *Rate sensitivity and inertia*

Generally energy absorbing structures are classified in two categories based on the shape of the load–displacement curve [27–29]. The structures exhibiting a relatively flat-topped load displacement curve are classified as Type I, while the structures exhibiting a steeply declining load-displacement curve as Type II. Examples of Type I structure include lateral compression of beams and tubes. Examples of Type II structures are axially loaded beams and tubes. Type II structure are more inertia and strain rate sensitive than Type I structures [27]. The tendency of energy absorption of Type II structures was shown to be enhanced by the structure material strain rate sensitivity [29].

The investigated combined geometry structure is a combination of a Type I structure (hemispherical portion) and a Type II structure (cylindrical portion). Therefore, the strain rate and inertia effects are expected to be different from constituents and combination of them. In order to investigate strain rate sensitivity and inertial effects; the crushing of combined geometry shells were numerical modeled at three different velocities, 50, 100, and 160 m/s, with and without including strain rate sensitivity. The force–displacement curves of the numerical simulations at 160 m/s impact velocity for the strain rate sensitive and insensitive models are shown seen in Fig. 12a together with the simulation force–displacement curve of quasi-static test. As seen in Fig. 12a, the force–displacement curves are divided in two portions, hemispherical and cylindrical, in order to identify the effects separately in individual portions of the combined geometry shell. The difference between the force values of strain rate sensitive and insensitive models can give the force increase from inertia. The determined inertial force values are then averaged as function of displacement for both hemispherical and cylindrical portions. As can be seen in Fig. 12a, both the strain rate and inertia sensitivities of the cylindrical portion are higher than those of hemispherical portion. It is also noted that inertia sensitivities of both portions are higher than strain rate sensitivities at 160 m/s impact velocity. The forces increase from inertia and strain rate sensitivity for both portions are determined as function velocity and shown in Fig. 12b. The force increase from inertia starts to begin to exceed the force increase from strain rate sensitivity at 100 m/s (Fig. 12b). It is also noted in Fig. 12b that the force increase from strain rate sensitivity on hemispherical portion is nearly equal for all of the impact velocities, while the force increase from strain rate sensitivity on cylindrical portion increases with increasing impact velocity. The results indicated clearly that there is a critical velocity for both constituents at which the effect of inertia in increasing crushing force becomes higher than that of strain rate sensitivity. Similar results of the effect of inertia and strain rate sensitivity were previously reported for a cellular material by Liu et al. [30].

In order to distinguish the effect of inertia, the simulations with and without strain rate sensitivity of steel alloy at constant energy were performed at different impact velocities. The simulation force–displacement deformation curves of quasi-static model and the strain rate insensitive and sensitive models at 50, 100 and 150 m/s are shown in Fig. 13a–c, respectively. A constant impact energy of 250 J produces a final displacement of 20 mm at quasi-static rate (Fig. 13a). The final displacements of strain rate insensitive model, which merely shows the inertial effects, are 19. 6, 17.98 and 16.5 mm at the impact velocities of 50, 100 and 150 m/s, respectively. The reduced final displacement at increasing impact velocities clearly indicates the inertial effects. The effect is also noted to increase with increasing impact velocity. With the use of strain rate sensitive model, the virtual displacements are further reduced; from 20 mm at quasi-static to 16.04, 14.9 and 13.68 mm at the impact velocities of 50, 100 and 150 m/s, respectively. The final deformation pictures of constant energy deformation models are shown in Fig. 13d. As can be seen in Fig. 13d, the effects of inertia and strain rate sensitivity are reflected as the reduced final displacements of the combined shell geometry. The effect of inertia in reducing the final displacement becomes more pronounced at increasing impact velocities as shown in Fig. 13d.

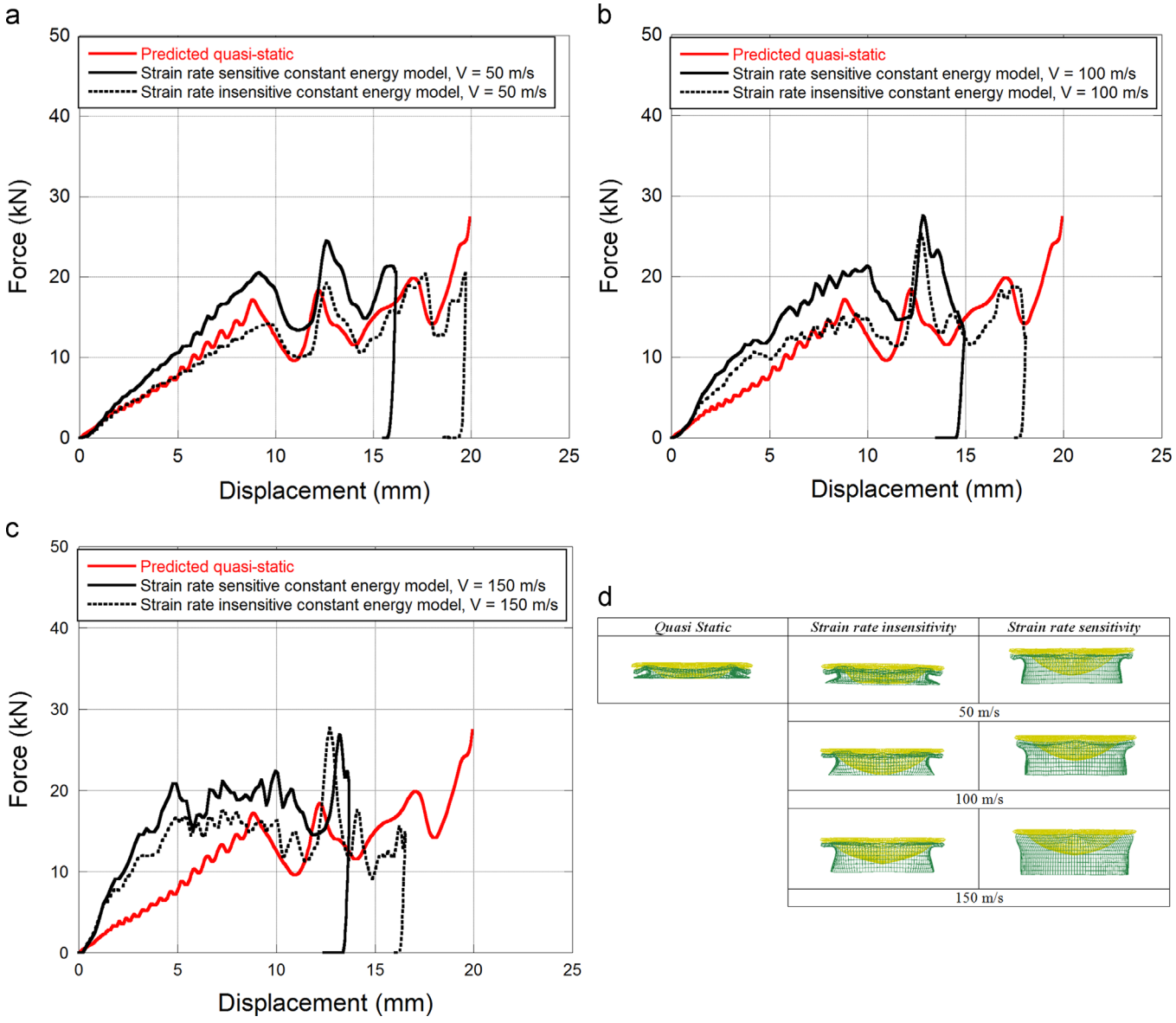

Fig. 13. Simulation force–displacement curves of quasi-static model and the strain rate insensitive and sensitive models at (a) 50, (b) 100 and (c) 150 m/s, (d) final deformation pictures of constant energy deformation models.

4. Conclusion

In this study, energy absorption characteristics of combined geometry shells composing of a hemispherical cap and cylinder segment were investigated at quasi-static and dynamic strain rates, experimentally and numerically. Based on experimental and numerical observations the following conclusions can be drawn:

- The combined geometry shell B1 was deformed in axisymmetric mode of deformation with the formation of folds in static regime, the deformation mode switched to diamond fold formation when deformation rate increased. The thicker specimen B2 fractured when strain rate increased.
- For the specimens having the same radius, as thickness increased, and P_m and *SAE* values increased. On the other hand, for the specimens of same thickness, as radius increased *SAE* values decreased and P_m values increased.
- *CFE* value decreased at the quasi-static strain rates, while it increased at dynamic strain rates as the thickness of the shell increased. For the specimens of the same thickness, *CFE value* increased with increasing radius at quasi static strain rates. On the other hand *CFE* decreased with increasing radius in dynamic loading.
- It was noted that the energy absorption by the hemispherical segment at high strain rate was greater than quasi-static strain rate. This could be attributed to the inertial effects.
- Average rate and inertia sensitivities were higher in cylindrical portion than those of hemispherical portion. For both of the constituents; inertia effect was higher than strain rate sensitivity at higher impact velocities.
- At higher impact velocities increase due to inertia effect was higher than that of strain rate. Strain rate effect of hemispherical portion was nearly independent of impact velocity. There was a critical velocity for both constituents at which effects of inertia became higher than effect of strain rate sensitivity.
- Higher impact velocities change the radius of folding, which resulted in a more inertia sensitive geometry at the same deformation level. It was also confirmed by comparing with and without strain rate sensitive models, deformed shapes

were nearly the same and as a result strain rate effects were very low at all impact velocities.

Acknowledgments

The authors would like to thank the Scientific and Technical Council of Turkey (TUBITAK) for the Grant # 112M141 and Prof.Dr. Mustafa Güden for his contributions.

References

[1] Alexander JM. An approximate analysis of the collapse of thin cylindrical shells under axial loading. Q J Mech Appl Math 1960;13:10–5.
[2] Abramowicz W, Jones N. Dynamic axial crushing of circular tubes. Int J Impact Eng 1984;2:263–81.
[3] Singace AA, El-Sobky H. Uniaxial crushing of constrained tubes. Mech Eng C 2001;215:353–64.
[4] Santosa SP, Wierzbicki T, Hanssen AG, Langseth M. Experimental and numerical studies of foam-filled sections. Int J Impact Eng 2000;24:509–34.
[5] Guden M, Kavi H. Quasi-static axial compression behavior of constraint hexagonal and square-packed empty and aluminum foam-filled aluminum multi-tubes. Thin Wall Struct 2006;44:739–50.
[6] Tasdemirci A. The effect of tube end constraining on the axial crushing behavior of an aluminum tube. Mater Des 2008;29:1992–2001.
[7] Shahi VJ, Marzbanrad J. Analytical and experimental studies on quasi-static axial crush behavior of thin-walled tailor-made aluminum tubes. Thin Wall Struct 2012;60:24–37.
[8] Updike DP. On the large deformation of a rigid-plastic spherical shell compressed by a rigid plate. J Manuf Sci Eng 1972;94:949–55.
[9] Deoliveira JG, Wierzbicki T. Crushing analysis of rotationally symmetric plastic shells. J Strain Anal Eng 1982;17:229–36.
[10] Gupta NK, Sheriff NM, Velmurugan R. Experimental and theoretical studies on buckling of thin spherical shells under axial loads. Int J Mech Sci 2008;50:422–32.
[11] Gupta NK, Venkatesh. Experimental and numerical studies of dynamic axial compression of thin walled spherical shells. Int J Impact Eng 2004;30:1225–40.
[12] Gupta PK, Gupta NK. Computational and experimental studies of crushing of metallic hemispherical shells. Arch Appl Mech 2006;76:511–24.
[13] Gupta NK, Sheriff NM, Velmurugan R. Experimental and numerical investigations into collapse behaviour of thin spherical shells under drop hammer impact. Int J Solids Struct 2007;44:3136–55.
[14] Ruan HH, Gao ZY, Yu TX. Crushing of thin-walled spheres and sphere arrays. Int J Mech Sci 2006;48:117–33.
[15] Dong XL, Gao ZY, Yu T. Dynamic crushing of thin-walled spheres: an experimental study. Int J Impact Eng 2008;35:717–26.
[16] Bao RH, Yu TX. Impact crushing and rebound of thin-walled hollow spheres. Key Eng Mater 2013;535-536:40–3.
[17] Ghamarian A, Abadi MT. Axial crushing analysis of end-capped circular tubes. Thin Wall Struct 2011;49:743–52.
[18] Ghamarian A, Zarei HR, Abadi MT. Experimental and numerical crashworthiness investigation of empty and foam-filled end-capped conical tubes. Thin Wall Struct 2011;49:1312–9.
[19] Ghamarian A, Zarei H. Crashworthiness investigation of conical and cylindrical end-capped tubes under quasi-static crash loading. Int J Crashworthines 2012;17:19–28.
[20] Gupta, P.K., Axial compression of tubular metallic shells having combined tube-frusta geometry, in: Proceedings of the International Conference on Structural Engineering, Construction and Management (ICSECM-2011), Sri Lanka, 2011.
[21] Ghamarian A, Zarei HR, Farsi MA, Ariaeifar N. Experimental and numerical crashworthiness investigation of the empty and foam-filled conical tube with shallow spherical caps. Strain 2013;49:199–211.
[22] Shojaeefard MH, Najibi A, Anbarloei M, Yeganeh M. Experimental and numerical crashworthiness investigation of combined circular and square sections. J Mech Sci Technol 2014;28:999–1006.
[23] Çakırcalı M, Kılıçaslan C, Güden M, Kıranlı E, Shchukin V, Petronko V. Cross wedge rolling of a Ti_6Al_4V (ELI) alloy: the experimental studies and the finite element simulation of the deformation and failure. Int J Adv Manuf Technol 2013;65:1273–87.
[24] LSTC, LS-DYNA: Keyword user's manual, livermore software technology corporation, in, LSTC, 2007.
[25] Maker, Z., A procedure for springback analysis using LS-DYNA.
[26] Mamalis AG, Johnson W. The quasi-static crumpling of thin-walled circular cylinders and frusta under axial compression. Int J Mech Sci 1983;25:713–32.
[27] Calladine CR, English RW. Strain-rate and inertia effects in the collapse of two types of energy-absorbing structure. Int J Mech Sci 1984;26:689–701.
[28] Zhang TG, Yu TX. A note on a 'velocity sensitive' energy-absorbing structure. Int J Impact Eng 1989;8:43–51.
[29] Tam LL, Calladine CR. Inertia and strain-rate effects in a simple plate-structure under impact loading. Int J Impact Eng 1991;11:349–77.
[30] Liu YD, Yu JL, Zheng ZJ, Li JR. A numerical study on the rate sensitivity of cellular metals. Int J Solids Struct 2009;46:3988–98.